



4.5- $\mu\text{m}$ -diameter latex beads, large enough to prevent slippage through the mesh. The cells spread and start contracting the surrounding network within 4 h (Fig. 1A). We probe the local micro-mechanics of the matrix using optical tweezers to pull these beads away from the cell at a constant speed of 1  $\mu\text{m/s}$  (Fig. 1B–D and *SI Appendix*, Fig. S1). This low speed ensures that the viscous drag on the bead from the background fluid is negligible compared with the network's restoring force, and at this speed the mechanical response of the matrix is rate independent, fully reversible, and therefore predominately elastic (*SI Appendix*, Fig. S2). Thus, this protocol enables us to obtain the local force–displacement relationship  $F(x)$  that characterizes the micromechanics of the matrix.

By probing a bead located far from the cell ( $>200 \mu\text{m}$ ), we determine the intrinsic response of the collagen matrix. The resulting force–displacement relationship is shown by the black line in Fig. 1E. The nonlinear differential stiffness  $k_{\text{nl}}(F) = dF/dx$ , defined as the slope of this force–displacement curve, increases with applied force  $F$ , revealing a strong force-stiffening behavior. This is reminiscent of the well-characterized stress-stiffening behavior measured at large scales using macrorheology on collagen gels (14, 34).

Interestingly, the matrix becomes substantially stiffer closer to the MDA-MB-231 cell (Fig. 1E). Indeed, the local linear stiffness  $k_{\text{lin}}$  of the matrix, defined as the small force limit of  $k_{\text{nl}}(F)$ , is two orders of magnitude larger near the cell than at a remote location (Fig. 1F, red squares). This direct observation of cell-induced matrix stiffening in the bulk of the network is consistent with prior 2D experiments showing cell-induced stiffening of the surface of a collagen matrix with a cell migrating on top (22), as well as with simulations (23).

This dramatic stiffness gradient in the vicinity of the cell originates from the active forces it exerts together with the nonlinear elasticity of the matrix. To demonstrate this, we first note that we can rule out the effect of the passive rigidity of the cell on the matrix stiffness, which is proven theoretically to be very short-ranged in 3D (33). Next, we measure the stiffness gradient around MCF-10A cells, a normal human mammary epithelial cell type with weak contractility. In this case, we observe negligible stiffening of the surrounding matrix (Fig. 1F, light blue polygons), in stark contrast to their highly contractile counterpart. Furthermore,

inhibiting cell contractility of MDA-MB-231 cells using 2  $\mu\text{M}$  cytochalasin D results in a strong attenuation of the cell-induced stiffening (Fig. 1F, blue circles). The weak residual stiffness gradient we observe with weakly contractile cells is well explained by increased ECM density near the cell, under the assumption that the matrix rigidity scales as the square of the collagen concentration  $c$  (36); by estimating  $c$  using confocal reflection microscopy, we determine that the enhanced matrix density near the cell can account for a stiffening of up to a factor of  $\sim 3$  (Fig. 1F, gray diamonds). However, the enhanced matrix concentration near the cell clearly cannot account for the much larger stiffness gradient generated by contractile MDA-MB-231 in collagen (Fig. 1F). Macrorheology experiments show that the stiffness of collagen gels increases not only with collagen concentration but also with stress (34). To test whether this nonlinear matrix response can account for the large stiffness gradient induced by the cell, we measure the local matrix stiffness in the vicinity of a MDA-MB-231 cell in a linear elastic matrix (37) with a similar macrorheological linear modulus to that of collagen (RGD-alginate, 5 mg/mL). In this linear elastic matrix, we observe no local stiffening effect around contracting cells (*SI Appendix*, Fig. S5). Taken together, our results demonstrate that active forces exerted by the cell result in an extended stiffened region in the 3D collagen matrix, reflecting the presence of a stress field decaying away from the cell with stress values sufficiently large to excite the nonlinear response of the collagen network, as illustrated in Fig. 1D.

### Nonlinear Stress Inference Microscopy

To study the cell-induced stress fields, we use the network's nonlinear microrheological response to our advantage and infer local stress values from our stiffness measurements. The nonlinear stiffening evidenced in Fig. 1E originates from two contributions: the force  $F$  exerted by the optical tweezers acting on the bead, and the local stress  $\sigma_{\text{loc}}$  induced by the cell. This similar influence of force and stress suggests that we may be able to extract  $\sigma_{\text{loc}}$  at a specific distance from the cell by comparing the corresponding force–displacement relationship to the remote measurement at which  $\sigma_{\text{loc}}$  is negligible. This comparison is confounded, however, because of force and stress being fundamentally different quantities:

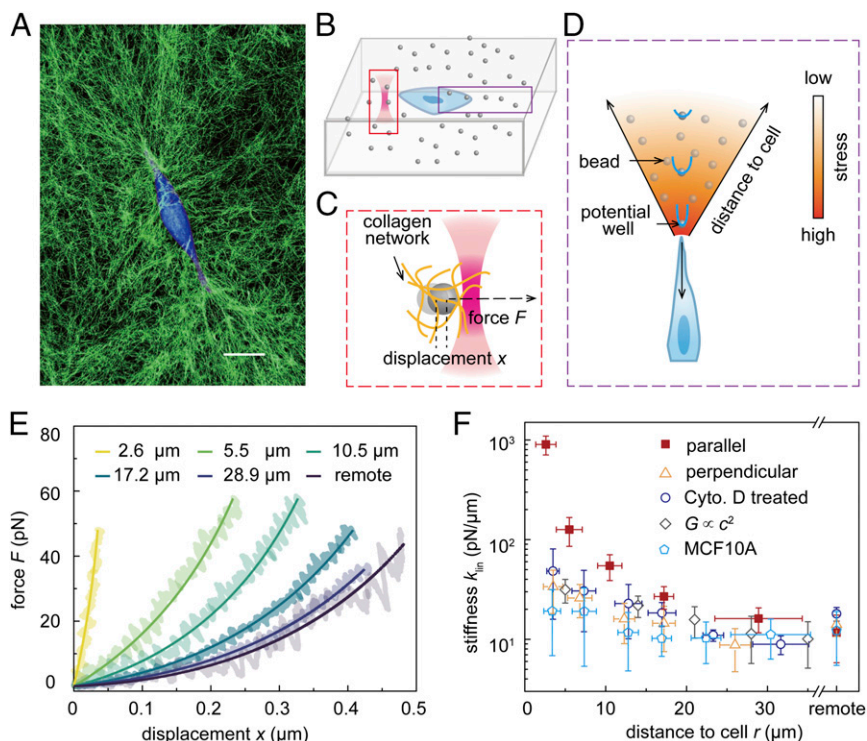


**Fig. 1.** Far-reaching stiffness gradient of ECM caused by a single contracting cell in a 3D collagen network. (A) Image of a MDA-MB-231 cell (blue) in a 3D collagen network (green). (Scale bar, 10  $\mu\text{m}$ .) (B–D) Schematics illustrating the force–displacement measurement with laser tweezers and the relation between matrix stiffening (blue potential wells) and the cell-generated stress field in the cell contraction direction. (E) Local force–displacement curves, showing the local nonlinear stiffening response in the collagen network. Different colors represent measurements at various distances from the cell along the contraction direction. (F) Quantification of the linear stiffness  $k_{\text{lin}}$  of the local 3D matrix as a function of distance to the cell  $r$ . Red squares and yellow triangles represent measurements along and perpendicular to the main contraction direction of MDA-MB-231 cells, respectively. Blue circles are measured along the contraction direction of MDA-MB-231 cells but with cell contraction inhibited by cytochalasin D treatment. Gray diamonds indicate the stiffness expected solely from the increased collagen concentration  $c$ . Light blue polygons represent measurements in the contraction direction of MCF-10A cells. Here, “remote” stands for the locations that are far away from the cell ( $>200 \mu\text{m}$ ), where the matrix's response is not affected by cell contraction. Error bars represent SD ( $n = 15$ ).

beyond having different dimensions, force transforms as an axial vector under spatial symmetry operations, while stress is a rank 2 tensor. This has an essential implication for the difference in the nonlinear response due to a force as opposed to a stress: The local stiffness should be invariant under reversal of the force vector,  $F$  to  $-F$ , while reversal of the stress tensor  $\sigma$  to  $-\sigma$  exchanges compression and tension, which can have a qualitatively different effect on the nonlinear mechanical response.

Despite these differences, here we show that a correspondence between force and stress controlled stiffening can be established in the strongly nonlinear regime. First, consider a simple 1D system of nonlinear springs representing the network surrounding a bead in a geometry with fixed network stress  $\sigma$  (Fig. 2A) and one with fixed tweezer force  $F$  (Fig. 2B). For nonlinear springs that stiffen under tension and soften under compression—a generic characteristic of biopolymers (14, 18, 38)—we find that the functional form of the stiffness curves actually becomes similar at large  $\sigma_{\text{loc}}$  and  $F$ , despite being qualitatively different in the weakly nonlinear regime. Indeed, the tensed spring in Fig. 2B dominates the differential stiffness experienced by the bead in the strongly nonlinear regime, rendering this case similar to the stress-controlled geometry, where the mechanical response is equally shared by two similarly tensed bonds (Fig. 2A). This quantitative similarity between the  $k_{\text{lin}}$  vs.  $\sigma_{\text{loc}}$  and  $k_{\text{nl}}$  vs.  $F$  curves in the strongly nonlinear regime enables us to use the latter, which we measure by nonlinear microrheology, as a “dictionary” to infer local stresses.

This intuitive correspondence between the force- and stress-controlled geometries in the nonlinear regime becomes mathematically exact when the springs’ differential stiffness has a power-law dependence on tension, as widely observed for biopolymer networks (34, 39) (SI Appendix, section 4). Specifically, from a measurement of  $k_{\text{lin}}$  in a network with an unknown local stress  $\sigma_{\text{loc}}$ , we can obtain an effective force  $F_{\text{eff}}$  defined such that  $k_{\text{nl}}(F_{\text{eff}}) = k_{\text{lin}}(\sigma_{\text{loc}})$ , and this effective force is directly proportional to the local stress:

$$\sigma_{\text{loc}} \approx a F_{\text{eff}}, \quad [1]$$

provided large local stresses, such that  $k_{\text{lin}} \gg k_0$ , where  $k_0$  is the linear stiffness of the unstressed network. We determine the proportionality factor  $a$  by assuming that nonlinearity sets in at a similar stress  $\sigma^*$  at a macro and microscopic level. In practice, we adjust  $a$  to match the low- and high-stress asymptotes, in a log–log plot, of the macroscopic differential shear modulus  $K$  ( $\sigma_{\text{macro}}$ ) to those of the microrheology curve  $k_{\text{nl}}(F)$  (Fig. 2 C–E and SI Appendix, Figs. S7 and S13). Together with Eq. 1, this provides a procedure to infer stresses from nonlinear microrheology, which we term nonlinear stress inference microscopy (NSIM).

To demonstrate the validity and accuracy of NSIM, we perform simulations of the experimental scenario presented in Fig. 1. We embed a contractile cell in a disordered 3D network of fibers with power-law stiffening (SI Appendix, section 2). We model the cell as a rigid ellipsoidal body that contracts along its long axis, inducing strong stiffening in an extended conic region as depicted in Fig. 3A. We then simulate a microrheology experiment by applying a force on a selection of network nodes to obtain a local force–displacement curves at various distances  $r$  along the contraction direction of the cell (Fig. 3B). From this, we determine the linear stiffness  $k_{\text{lin}}$  of the network as a function of  $r$  (Fig. 3C), which exhibits a dependence similar to the experimental measurements shown in Fig. 1F. We further confirm that this dependence vanishes in the direction perpendicular to contraction and in the absence of an active contractile force, as in experiments (Fig. 1F). We infer the local stress field from these linear stiffnesses using NSIM, as shown in Fig. 3D. We find excellent agreement with the “true” local stress in the strong stiffening regime even when mechanical disorder gives rise to fluctuations in the stress field (Fig. 3E and SI Appendix, section 3), thereby validating NSIM as a quantitative method to capture the spatial stress distribution around a contractile cell in a disordered 3D fiber matrix (Fig. 3D–F).

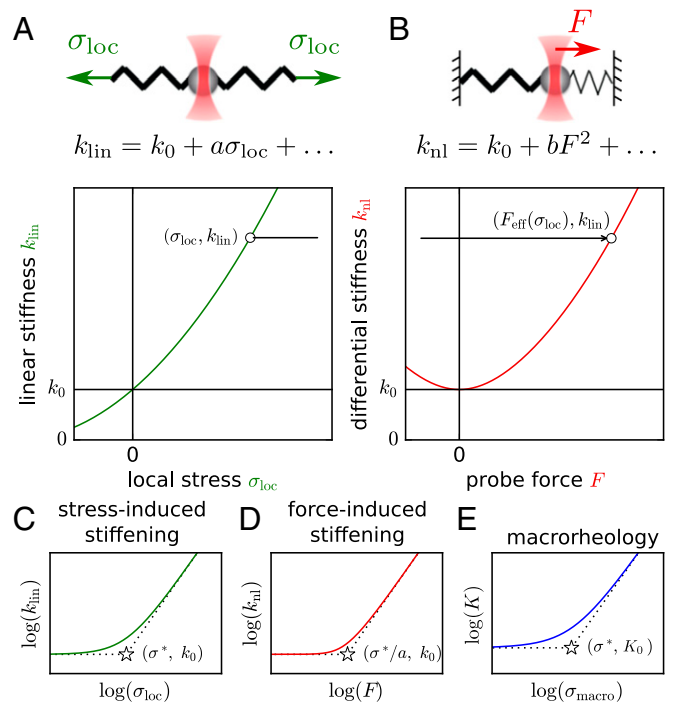


**Fig. 2.** Nonlinear elastic responses can be used to infer cell-induced local stresses. (A) One-dimensional system of nonlinear springs in a stress-controlled geometry with local stress  $\sigma_{\text{loc}}$ . (B) Force-controlled geometry with force  $F$  applied to the central bead, together with an expansion of stiffness dictated by symmetry properties of the two scenarios and a schematic of the nonlinear response. The linear stiffness,  $k_{\text{lin}}$ , of the system in A can be measured by applying a small perturbation to the central bead, while the nonlinear stiffness,  $k_{\text{nl}}$ , is defined as the derivative of the force–displacement curve of the central bead in B. The springs represent the surrounding network. (C) Schematics of linear microrheological stiffness as a function of the local stress in the stress-controlled geometry on a logarithmic scale. (D) Nonlinear microrheological stiffness for the force-controlled geometry. (E) Differential shear modulus,  $K$ , as a function of applied shear stress  $\sigma_{\text{macro}}$  as in a macroscopic rheology experiment. Our inference technique exploits a correspondence between the stress-controlled and force-controlled geometries in the strongly nonlinear regime.

### Tensile Stress Propagation Leads to Extended Stiffness Gradients Around Cells

To unravel the mechanical origins of the far-reaching cell-induced stiffness gradient in collagen (Figs. 1F and 4A), we use NSIM to experimentally infer the local stresses  $\sigma_{\text{loc}}(r)$  around a cell inside the matrix. The inferred stress decays with distance  $r$  from the cell consistent with a power law  $\sigma_{\text{loc}} \sim r^{-2}$  (Fig. 4B), in contrast with the power law  $\sigma_{\text{loc}} \sim r^{-3}$  expected in the far field for a linear material (40). Our model-independent measurement of slow stress decay is consistent with previous theoretical predictions for models of fiber networks with various nonlinear force–extension relationships (41–44), as well as with the observed deviations from linear elasticity in experimental deformation fields (23, 29). Importantly, however, in this specific geometry where an elongated cell exerts opposite forces at two distant points (5, 23, 29), near-field linear elasticity also predicts an inverse quadratic stress decay at distances smaller than the cell diameter, rendering it difficult to distinguish linear and nonlinear force transmission. Nevertheless, our simulations predict that this long-ranged decay extends further than the cell size, showing a clear deviation from the linear elastic prediction (Fig. 3F).

Conceptually, this increased range of stresses in fibrous materials found in simulation results from their asymmetric response to tension and compression: Fibers stiffen under tension and soften due to buckling under compression (18, 45). Simply speaking, the matrix around a strong contractile cell effectively behaves as a network of ropes, where only tensile forces are transmitted,

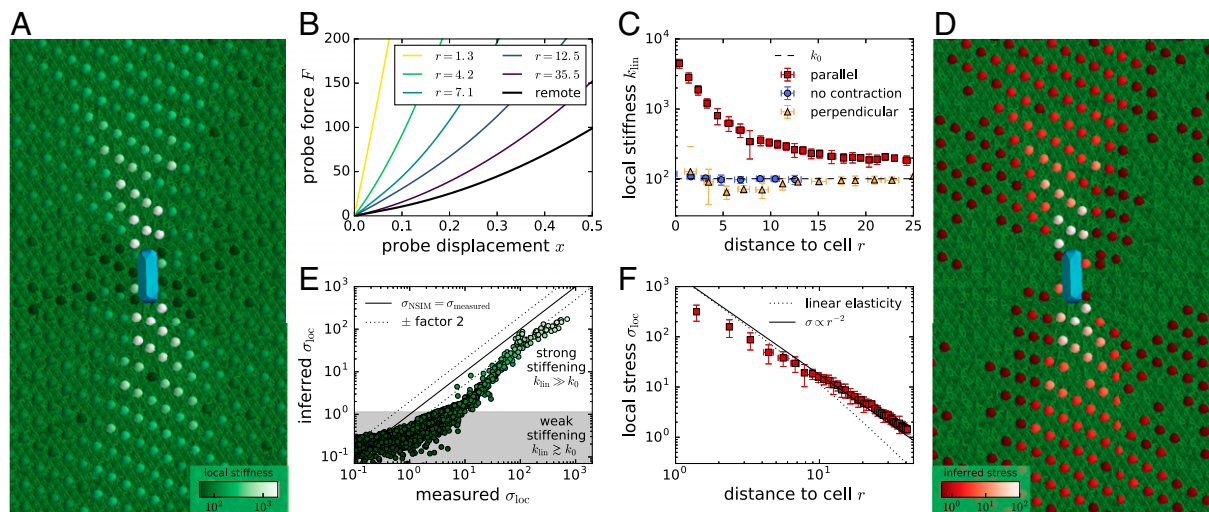


**Fig. 3.** Three-dimensional simulations of cell-generated stress fields inducing nonlinear network response and validations of NSIM. (A) Simulated rigid ellipsoidal cell contracting inside a 3D nonlinear fiber network (in green). The linear stiffness  $k_{lin}$  is depicted by the spheres in a green-white logarithmic color gradient. (B) Local force-displacement curves, showing the local nonlinear stiffening response in the simulated network. Different colors represent measurements at various distances from the cell along the contraction direction. (C) Local linear stiffness  $k_{lin}$  of the 3D matrix as a function of distance to the cell  $r$  from simulations. Red and yellow symbols represent data parallel and perpendicular to the main contraction direction, respectively. Blue symbols correspond to a noncontracting rigid cell. (D) The inferred stress depicted by spheres in a red-white logarithmic color gradient in the same simulation as in A. Absent points along the direction perpendicular to the cell's contraction axis correspond to soft compressed regions where the local stiffness is smaller than  $k_0$ , precluding the use of NSIM. (E) Inferred stresses from simulated data in B using NSIM vs. direct numerically determined stress, demonstrating that NSIM allows to correctly infer stresses within a factor of order 1 in the nonlinear regime. (F) The local stress along the cell axis decays as  $r^{-2}$ , faster than the linear elastic prediction in this geometry (dotted line).

unimpeded by orhothradial compressive counterforces. Hence the total contractile force exerted by the cell is conserved with distance, and the decay of radial stress simply reflects this force spreading over an increasing surface area (41). This buckling-based mechanism for long-range stress transmission is supported by observations with confocal reflection microscopy of a larger amount of highly curved collagen filaments in the vicinity of a contractile cell, compared with the case where contraction is inhibited with cytochalasin D (Fig. 4 E and F).

To explore the generality of our observations in collagen, we perform the same nonlinear microrheological experiments with MDA-MB-231 cells in a 2.5 mg/mL Matrigel (Fig. 4A, green circles), a blend of biopolymers more complex than pure collagen (46), and for human umbilical vein endothelial cells (HUVECs) in a 3.0 mg/mL fibrin gel (light blue triangles in Fig. 4A). In both cases, we find that cells are capable of generating large extended stiffness gradients along the cell's contraction direction (Fig. 4A). Using NSIM, we find that the slow stress decay consistent with rope-like force transmission ( $\sigma_{loc} \sim r^{-2}$ ) is observed in all three cases, despite significant variability in the absolute magnitude of the stresses (solid lines in Fig. 4B). The stresses induced by the cell enhance the linear stiffness  $k_{lin}$  over an extended region of the ECM (Figs. 1F and 4A), thus exciting the nonlinear elastic response of the matrix over a distance exceeding the cell size. These results also highlight the wide applicability of NSIM.

Cells actively modify not only the linear stiffness of their 3D matrix environment (Fig. 4A) but also the nonlinear mechanical response. To reveal how cell stress and probe forces combine to stiffen the surrounding network, we measure the full nonlinear microrheological response of the network both in the vicinity of the cell and at a remote location in all three types of ECM model systems, as shown in Fig. 4C. The nonlinear  $k_{nl}$  vs.  $F$  curves measured at different distances from the cell are clearly separated from the remote measurement. This observation cannot be accounted for by network heterogeneities (SI Appendix, Fig. S3) or the increase of network concentration near the cell (SI Appendix, Fig. S4), indicating a significant contribution of cell-generated stress on the nonlinear mechanical response. This contribution could be through nonlinear network elastic stiffening or network plastic deformation (47). We note that our

stress inference is largely independent of the specifics of the ECM's nonlinear response but does assume a predominantly elastic response to the forces generated by the cell. Indeed, significant plastic deformations could imply that the ECM's nonlinear response is systematically modified as a function of the distance from the cell. In the absence of plastic deformations, we expect that further stiffening a prestressed matrix by a large tweezer force would result in a nonlinear response that is functionally similar for all levels of cell stress. To test this, we plot all nonlinear stiffening curves as a function of the combined force  $F + F_{eff}$ , where the effective force  $F_{eff} \propto \sigma_{loc}$  is determined as in Fig. 2A and B (SI Appendix, Table S1). Remarkably, we find that the data taken at different distances to the cell collapse in any network composition onto a smooth master curve (Fig. 4D). The large cell-generated stress thus locally drives the ECM into an elastic nonlinear regime, which can be further extended by the probe force we apply with optical tweezers.

Several studies have reported experimentally measured displacement fields induced by a contracting cell in 3D contexts (23, 29, 30, 35, 48, 49). By using these displacement fields together with a continuum elasticity model, it was suggested that the matrix may stiffen near the cell. However, to our knowledge, no direct measurements of the local stiffness have been done in 3D contexts, at the scale of a cell level. Furthermore, we infer the stresses responsible for this stiffening using NSIM, a conceptually unique inference technique that does not require knowledge of the materials' constitutive stress-strain relationship nor of a reference undeformed state. Due to its simplicity and insensitivity to the detailed material's properties, NSIM could be used in various conditions, including embryo or tumor development. The stresses inferred using this technique far from the cell are consistent with prior measurements (29). Close to the cell, strong stiffening renders the technique most accurate and corresponds to stresses of the order of 200 Pa, larger than previously reported (29). These cell-induced stresses decay more slowly than in a linear continuum material, which can be accounted for by buckling of fibers in the network, impeding the transmission of compressive stresses. This slow stress decay has also been inferred in previous studies by using a finite-element model in conjunction with imaged deformation fields (23, 29). Here, we provide direct evidence for

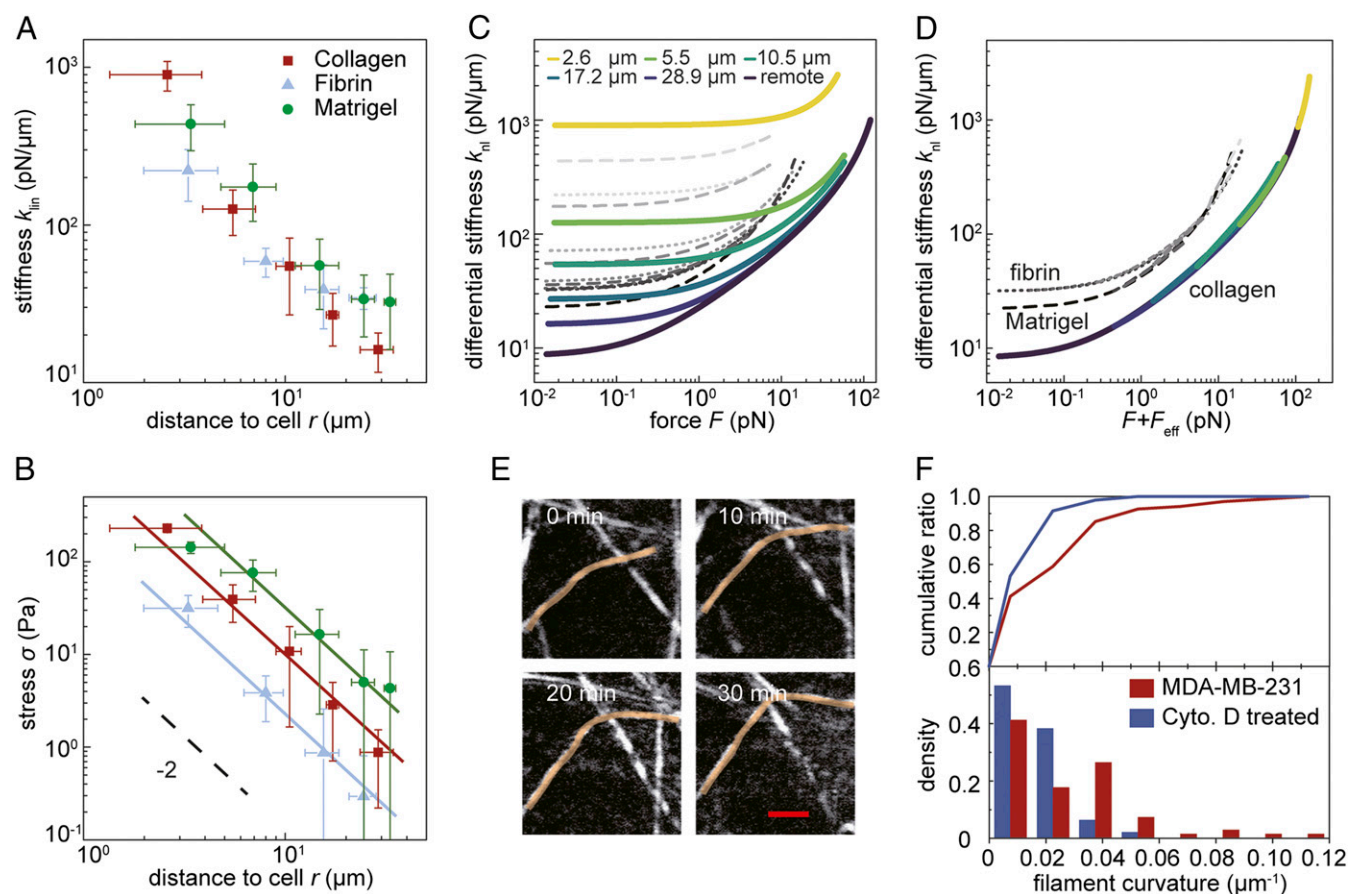


**Fig. 4.** Nonlinear matrix stiffening and cell-generated stress propagation in various 3D biopolymer networks. (A) Local linear stiffness  $k_{lin}$  is plotted against the distance to the cell  $r$  along its principal contraction direction in collagen (red square), fibrin (blue triangle), and Matrigel (green circle). All three different ECM model systems exhibit a strong cell-induced stiffening gradient. (B) The stress field  $\sigma$  generated by the cell determined using NSIM is shown as a function of distance to the cell  $r$ , and the dashed line indicates a slope of  $-2$ . (C) Local nonlinear differential stiffness  $k_{nl}$  is plotted against the applied probe force  $F$  for all three ECM model systems. (D) Collapse of the data from C onto a master curve in each respective matrix obtained by plotting  $k_{nl}$  as a function of combined local force  $F + F_{eff}$ , where the  $F_{eff}$  is determined using NSIM. (E) Time-lapse imaging shows the buckling process of a single fiber around a contracting cell. The fiber undergoing buckling is highlighted in yellow. (Scale bar, 2  $\mu\text{m}$ .) (F) Fiber curvature distributions (Bottom) and the cumulative probability (Top) near the cell, within a 60- $\mu\text{m}$  distance along the principal cell contraction direction, before and after cytochalasin D treatment. Error bars in A and B represent SD ( $n = 15$ ).

long-range stress transmission by using a model-independent measurement of local stresses and their decay around a cell. These cell-induced stresses result in far-reaching stiffness gradients as high as 50 Pa/ $\mu\text{m}$  over a cell diameter. Other cells in the surrounding matrix could sense and respond to such large gradients, suggesting that cell-induced ECM stiffening could mediate intercell mechanical communication and collective durotaxis. These observations highlight the critical role of nonlinear matrix mechanics not only in shaping cell–ECM interactions (8, 50) but also for matrix-mediated interactions between cells.

## Methods

**Cell Culture and Matrix Preparation.** Cells are maintained under 37  $^{\circ}\text{C}$ , 5%  $\text{CO}_2$  and 95% humidity. MDA-MB-231 cells were cultured in DMEM with 10% FBS, 1% penicillin and streptomycin. HUVECs (Lonza) were cultured on collagen I-coated flasks in EGM-2 growth medium (Lonza) and used between passages 6 and 8. To prepare the collagen gel, 800  $\mu\text{L}$  of type I bovine collagen solution (3.0 mg/mL; PureCol; Advanced BioMatrix) was mixed with 100  $\mu\text{L}$  of PBS (10 $\times$ ). We adjusted the solution to pH 7.2 with  $\sim 70$   $\mu\text{L}$  of 0.1 M NaOH. The collagen solution is then mixed with PBS (1 $\times$ ) to reach a final collagen concentration of 1.5 mg/mL and polymerized in the cell culture incubator for 30 min. To prepare the fibrin gel, fibrinogen from bovine plasma (F8630; Sigma) was dissolved in PBS at 6 mg/mL. Thrombin (T4648; Sigma) was dissolved at 2 U/mL in PBS (for experiments without cells) or in EGM-2 (for experiments with cells). Then we mixed thrombin and fibrinogen at 1:1 volume ratio and polymerized it in the cell culture incubator for 15 min. For Matrigel preparation, the basement

membrane matrix (10 mg/mL; Corning) was diluted to 2.5 mg/mL with DMEM and polymerized in the cell culture incubator for 30 min. For all cell-loaded gels, cell and bead suspensions were added to the gel solution before polymerization, with a cell density around  $10^4/\text{mL}$ , and all measurements were conducted 12 h after polymerization. To inhibit contractility of MDA-MB-231 cells, we disrupted filamentous actin structures using 2  $\mu\text{M}$  cytochalasin D (PHZ1063; Invitrogen) for 30 min.

**Optical Tweezer Measurements.** We used a Thorlabs optical tweezers system to perform all measurements. Briefly, to optically trap a bead (4.5- $\mu\text{m}$  carboxylate microspheres; Polyscience) that is embedded and confined in a 3D biopolymer network, the laser beam (5 W, 1,064 nm) is tightly focused through a series of Keplerian beam expanders and a high-N.A. objective (100 $\times$  1.4; oil; Leica). A high-resolution quadrant detector was used for position detection. The linear region of the detector and the trap stiffness (0.04 pN/nm) were calibrated with the same bead in pure cell culture media by using an active power-spectrum method and equipartition theorem (51). To manipulate the trapped bead, a high-resolution piezo stage (P-545; PI nano) was moved at a constant velocity of 1  $\mu\text{m}/\text{s}$ , and the relative distance between laser and bead was recorded, from which local force–displacement curves inside the matrix were determined (52) (see *SI Appendix* for details).

**Bulk Rheology.** We performed bulk rheology measurements on a DHR-3 rheometer (TA Instruments) using a plate–plate geometry, with a 40-mm glass disk as the top plate and a 60-mm Petri dish as the bottom plate with a gap of 500  $\mu\text{m}$ . All gels were formed in the gap at 37  $^{\circ}\text{C}$  and were sealed by mineral oil to avoid evaporation. The polymerization process was monitored

by strain oscillations with a strain amplitude of 0.005 at a frequency of 1 rad/s. After polymerization, a strain ramp was applied to the gel at a rate of 0.01/s, and the resulting stresses were measured.

**Theoretical Modeling and Simulations.** Numerical simulations presented in Fig. 3 are performed using a model of nonlinear springs [force–extension relation  $f(x) = \exp(\mu x) - 1$ ; see *SI Appendix, Figs. S10 and S11* for other types of nonlinearities], with regular removal of springs to introduce disorder in the network, while ensuring a fiber length  $L_f = 10$ , in a spherical system of radius  $R = 50.5$ . The contractile cell is a rigid ellipsoidal body of size  $14.2 \times 2.8 \times 2.8$ , with force and torque balance, contracted by 50% along its long axis. The surrounding network is flexibly clamped at the surface of the cell and at the boundary of the system. Mechanical equilibrium is attained by minimization of the energy using the BFGS algorithm. Further details are provided in *SI Appendix, sections 2 and 3*.

**Imaging of Collagen Networks and Image Analysis.** The 3D collagen networks near a contracting cell were imaged with confocal reflection microscopy using a 63 $\times$ , 1.2 N.A. water objective (Leica SP8). To determine the boundary of the cell, the cytoplasm was stained with CellTracker Green (C7025; Thermo Fisher) and imaged at the same time under confocal microscope. To capture the fiber buckling process, we imaged the cell and its surrounding 3D fiber

networks at a 5-min interval for 4 h at 37 °C and with 5% CO<sub>2</sub>. To analyze the curvature of single collagen fiber, we manually selected 20 points on each individual collagen fiber; the fiber outline was determined by cubic spline interpolation, from which the average curvature of the fiber was calculated.

**ACKNOWLEDGMENTS.** We thank Anna Posfai for useful comments. This work was supported by National Cancer Institute Grant 1U01CA202123 (to M.G.), the German Excellence Initiative via the program “NanoSystems Initiative Munich” (to C.P.B.) and DFG via project B12 within the SFB-1032 (to C.P.B.), a Princeton Center for Theoretical Science fellowship (to P.R.), and a Massachusetts Institute of Technology International Science and Technology Initiatives–Germany seed fund (to M.G. and C.P.B.). M.G. also acknowledges support from the Department of Mechanical Engineering at Massachusetts Institute of Technology. A.M. is supported by European Union’s Seventh Framework Programme for Research Grant 625500. M.L. was supported by Marie Curie Integration Grant PCIG12-GA-2012-334053, “Investissements d’Avenir” LabEx PALM Grant ANR-10-LABX-0039-PALM, Agence Nationale de la Recherche Grant ANR-15-CE13-0004-03, and European Research Council Starting Grant 677532. M.L.’s group belongs to the CNRS consortium CellTis. This work was performed in part at the Aspen Center for Physics, which is supported by National Science Foundation Grant PHY-1607611.

- Discher DE, Janmey P, Wang YL (2005) Tissue cells feel and respond to the stiffness of their substrate. *Science* 310:1139–1143.
- Discher DE, Mooney DJ, Zandstra PW (2009) Growth factors, matrices, and forces combine and control stem cells. *Science* 324:1673–1677.
- Mammoto A, Ingber DE (2009) Cytoskeletal control of growth and cell fate switching. *Curr Opin Cell Biol* 21:864–870.
- Angelini TE, Hannezo E, Trepat X, Fredberg JJ, Weitz DA (2010) Cell migration driven by cooperative substrate deformation patterns. *Phys Rev Lett* 104:168104.
- De R, Zemel A, Safran SA (2007) Dynamics of cell orientation. *Nat Phys* 3:655–659.
- Rehfeldt F, Discher DE (2007) Biophysics: Cell dipoles feel their way. *Nat Phys* 3:592–593.
- Nitsan I, Drori S, Lewis YE, Cohen S, Tzilil S (2016) Mechanical communication in cardiac cell synchronized beating. *Nat Phys* 12:472–477.
- Ahmadzadeh H, et al. (2017) Modeling the two-way feedback between contractility and matrix realignment reveals a nonlinear mode of cancer cell invasion. *Proc Natl Acad Sci USA* 114:E1617–E1626.
- Provenzano PP, et al. (2006) Collagen reorganization at the tumor-stromal interface facilitates local invasion. *BMC Med* 4:38.
- Bischofs IB, Schwarz US (2003) Cell organization in soft media due to active mechanosensing. *Proc Natl Acad Sci USA* 100:9274–9279.
- Trepat X, et al. (2009) Physical forces during collective cell migration. *Nat Phys* 5:426–430.
- Tambe DT, et al. (2011) Collective cell guidance by cooperative intercellular forces. *Nat Mater* 10:469–475.
- Griffith LG, Swartz MA (2006) Capturing complex 3D tissue physiology in vitro. *Nat Rev Mol Cell Biol* 7:211–224.
- Storm C, Pastore JJ, MacKintosh FC, Lubensky TC, Janmey PA (2005) Nonlinear elasticity in biological gels. *Nature* 435:191–194.
- Lieleg O, Claessens MM, Heussinger C, Frey E, Bausch AR (2007) Mechanics of bundled semiflexible polymer networks. *Phys Rev Lett* 99:088102.
- Gardel ML, et al. (2004) Elastic behavior of cross-linked and bundled actin networks. *Science* 304:1301–1305.
- Broedersz CP, Sheinman M, MacKintosh FC (2012) Filament-length-controlled elasticity in 3D fiber networks. *Phys Rev Lett* 108:078102.
- Broedersz CP, MacKintosh FC (2014) Modeling semiflexible polymer networks. *Rev Mod Phys* 86:995–1036.
- Onck PR, Koeman T, van Dillen T, van der Giessen E (2005) Alternative explanation of stiffening in cross-linked semiflexible networks. *Phys Rev Lett* 95:178102.
- Wyart M, Liang H, Kabla A, Mahadevan L (2008) Elasticity of floppy and stiff random networks. *Phys Rev Lett* 101:215501.
- Sharma A, et al. (2016) Strain-controlled criticality governs the nonlinear mechanics of fibre networks. *Nat Phys* 12:584–587.
- van Helvert S, Friedl P (2016) Strain stiffening of fibrillar collagen during individual and collective cell migration identified by AFM nanoindentation. *ACS Appl Mater Interfaces* 8:21946–21955.
- Hall MS, et al. (2016) Fibrous nonlinear elasticity enables positive mechanical feedback between cells and ECMs. *Proc Natl Acad Sci USA* 113:14043–14048.
- Shokef Y, Safran SA (2012) Scaling laws for the response of nonlinear elastic media with implications for cell mechanics. *Phys Rev Lett* 108:178103.
- Jansen KA, Bacabac RG, Piechocka IK, Koenderink GH (2013) Cells actively stiffen fibrin networks by generating contractile stress. *Biophys J* 105:2240–2251.
- Campàs O, et al. (2014) Quantifying cell-generated mechanical forces within living embryonic tissues. *Nat Methods* 11:183–189.
- Saha A, et al. (2016) Determining physical properties of the cell cortex. *Biophys J* 110:1421–1429.
- Nia HT, et al. (2016) Solid stress and elastic energy as measures of tumour mechanopathology. *Nat Biomed Eng* 1:0004.
- Steinwachs J, et al. (2016) Three-dimensional force microscopy of cells in biopolymer networks. *Nat Methods* 13:171–176.
- Legat WR, et al. (2010) Measurement of mechanical tractions exerted by cells in three-dimensional matrices. *Nat Methods* 7:969–971.
- Doyle AD, Carvajal N, Jin A, Matsumoto K, Yamada KM (2015) Local 3D matrix microenvironment regulates cell migration through spatiotemporal dynamics of contractility-dependent adhesions. *Nat Commun* 6:8720.
- Jones CAR, et al. (2015) Micromechanics of cellularized biopolymer networks. *Proc Natl Acad Sci USA* 112:E5117–E5122.
- Beroz F, et al. (2017) Physical limits to biomechanical sensing in disordered fibre networks. *Nat Commun* 8:16096.
- Licup AJ, et al. (2015) Stress controls the mechanics of collagen networks. *Proc Natl Acad Sci USA* 112:9573–9578.
- Stout DA, et al. (2016) Mean deformation metrics for quantifying 3D cell–matrix interactions without requiring information about matrix material properties. *Proc Natl Acad Sci USA* 113:2898–2903.
- MacKintosh FC, Käs J, Janmey PA (1995) Elasticity of semiflexible biopolymer networks. *Phys Rev Lett* 75:4425–4428.
- Zhao X, Huebsch N, Mooney DJ, Suo Z (2010) Stress-relaxation behavior in gels with ionic and covalent crosslinks. *J Appl Phys* 107:63509.
- Burkel B, Notbohm J (2017) Mechanical response of collagen networks to nonuniform microscale loads. *Soft Matter* 13:5749–5758.
- Gardel ML, et al. (2006) Prestressed F-actin networks cross-linked by hinged filamins replicate mechanical properties of cells. *Proc Natl Acad Sci USA* 103:1762–1767.
- Landau LD, Lifshitz EM (1987) *Course of Theoretical Physics* (Butterworth-Heinemann, Oxford).
- Ronceray P, Broedersz CP, Lenz M (2016) Fiber networks amplify active stress. *Proc Natl Acad Sci USA* 113:2827–2832.
- Wang H, Abhilash AS, Chen CS, Wells RG, Shenoy VB (2014) Long-range force transmission in fibrous matrices enabled by tension-driven alignment of fibers. *Biophys J* 107:2592–2603.
- Rosakis P, Notbohm J, Ravichandran G (2015) A model for compression-weakening materials and the elastic fields due to contractile cells. *J Mech Phys Solids* 85:16–32.
- Xu X, Safran SA (2015) Nonlinearities of biopolymer gels increase the range of force transmission. *Phys Rev E Stat Nonlin Soft Matter Phys* 92:032728.
- van Oosten AS, et al. (2016) Uncoupling shear and uniaxial elastic moduli of semiflexible biopolymer networks: Compression-softening and stretch-stiffening. *Sci Rep* 6:19270.
- Kleinman HK, Martin GR (2005) Matrigel: Basement membrane matrix with biological activity. *Semin Cancer Biol* 15:378–386.
- Kim J, et al. (2017) Stress-induced plasticity of dynamic collagen networks. *Nat Commun* 8:842.
- Mulligan JA, Bordeleau F, Reinhart-King CA, Adie SG (2017) Measurement of dynamic cell-induced 3D displacement fields in vitro for traction force optical coherence microscopy. *Biomed Opt Express* 8:1152–1171.
- Owen LM, et al. (2017) A cytoskeletal clutch mediates cellular force transmission in a soft, 3D extracellular matrix. *Mol Biol Cell* 28:1959–1974.
- Winer JP, Oake S, Janmey PA (2009) Non-linear elasticity of extracellular matrices enables contractile cells to communicate local position and orientation. *PLoS One* 4:e3382.
- Jun Y, Tripathy SK, Narayanareddy BR, Mattson-Hoss MK, Gross SP (2014) Calibration of optical tweezers for in vivo force measurements: How do different approaches compare? *Biophys J* 107:1474–1484.
- Hu J, et al. (2017) Size- and speed-dependent mechanical behavior in living mammalian cytoplasm. *Proc Natl Acad Sci USA* 36:9529–9534.